Forests **2014**, *5*, 2542-2560; doi:10.3390/f5102542

OPEN ACCESS

forests

ISSN 1999-4907

www.mdpi.com/journal/forests

Article

Impacts of Deforestation and Climate Variability on Terrestrial Evapotranspiration in Subarctic China

Yunjun Yao [1,*], Shunlin Liang [1,2], Jie Cheng [1], Yi Lin [3], Kun Jia [1] and Meng Liu [1]

[1] State Key Laboratory of Remote Sensing Science, College of Global Change and Earth System Science, Beijing Normal University, No.19 Xinjiekou Street, Beijing 100875, China; E-Mails: sliang@umd.edu (S.L.); brucechan2003@126.com (J.C.); jiakun@bnu.edu.cn (K.J.); xinyin_liumeng@163.com (M.L.)

[2] Department of Geographical Sciences, University of Maryland, College Park, MD 20742, USA

[3] Institute of Remote Sensing and GIS, Peking University, No.5 Yiheyuan Road, Beijing 100871, China; E-Mail: yi.lin@pku.edu.cn

* Author to whom correspondence should be addressed; E-Mail: yaoyunjun@bnu.edu.cn; Tel.: +86-10-5880-3002; Fax: +86-10-5880-9071.

External Editor: Eric J. Jokela

Received: 26 June 2014; in revised form: 6 October 2014 / Accepted: 20 October 2014 / Published: 23 October 2014

Abstract: Although deforestation affects hydrological and climatic variables over tropical regions, its actual contributions to changes in evapotranspiration (ET) over subarctic China remain unknown. To establish a quantitative relationship between deforestation and terrestrial ET variations, we estimated ET using a semi-empirical Penman (SEMI-PM) algorithm driven by meteorological and satellite data at both local and regional scales. The results indicate that the estimated ET can be used to analyse the observed inter-annual variations. There is a statistically significant positive relationship between local-scale forest cover changes (ΔF) and annual ET variations (ΔET) of the following form: $\Delta ET = 0.0377\Delta F - 2.11$ ($R^2 = 0.43$, $p < 0.05$). This relationship may be due to deforestation-induced increases in surface albedo and a reduction in the fractional vegetation cover (FVC). However, the El Niño/Southern Oscillation (ENSO), rather than deforestation, dominates the multi-decadal ET variability due to regional-scale wind speed changes, but the exact effects of deforestation and ENSO on ET are challenging to quantify.

Keywords: deforestation; evapotranspiration; subarctic China; climate variability

1. Introduction

Evapotranspiration (ET) is the flux of water transferred from the land surface to the atmosphere and is an important bio-geophysical parameter for determining variations in the global energy, hydrological and carbon cycles [1–7]. ET is primarily controlled by atmospheric evaporative demand, available energy, and vegetation and soil moisture supplies [8–12]. With the increase in global temperatures, atmospheric evaporative demand has been increasing in many regions of the world over the past several decades, which should result in increased ET [13,14]. However, the trend in ET may not be positive in some regions because land-use changes caused by anthropogenic activities are hypothesized to affect the available energy and moisture demands by altering biophysical processes that regulate ET [15–19]. Moreover, the effects of land-use changes, especially deforestation, on local and regional scale ET variations remain uncertain.

Deforestation is a type of land-use change that is caused by human activities. Moreover, deforestation has been linked to near-surface air temperature, surface albedo, radiative forcing, water vapour and ET changes, resulting in a warmer climate [20,21]. Previous work has shown that tropical deforestation in the Indochina Peninsula is a main cause of decreasing precipitation in September [22]. Amazonian deforestation has been shown to induce large-scale circulation changes in middle and high latitudes [23]. Other studies have shown that the conversion of forests to grasslands in both South America and central Africa leads to local regional climate responses [18,24,25]. Like many Arctic and tropical climate regions, subarctic China is highly vulnerable to changes in the energy, hydrological and carbon budgets. A small land-cover change can have large local climate and hydrological changes [19,20]. Therefore, it is essential to analyse the effects of deforestation on climatic and hydrological changes in subarctic China at different spatial scales.

Many scholars have examined the effects of de(re)forestation on climatic and hydrological variables in northern China using ground-based observation data and remote sensing products [16,20,26]. Gao and Liu [20] reported a critical deforestation threshold beyond which noticeable climate warming occurs at a scale of 5 km^2. Zhang and Liang [16] estimated the instantaneous net radiative forcing caused by logging to be 2.23 ± 0.27 W/m^2; moreover, they also found that the trajectories of CO_2-driven, albedo-driven and net radiative forcings exhibit temporal differences. Peng *et al*. [26] documented that afforestation in China has decreased daytime land surface temperatures (LSTs) by approximately 1.1 K and increased night-time LSTs by approximately 0.2 K. However, Jackson *et al*. [27] found the opposite effects in high-latitude regions. In subarctic China, the Chinese government has protected forests and enhanced the fraction of vegetation cover since the 1980s; the actual extent of deforestation is severe because local farmers' logging activities are intended to achieve economic objectives [20,28]. However, little information is known about the effects of deforestation on terrestrial ET in subarctic China due to limited data availability. Moreover, it is unclear how terrestrial ET in subarctic China responds to climate change at different regional scales over long time periods.

In this study, we attempt to establish a quantitative relationship between deforestation/climate variability and terrestrial ET variations in subarctic China. Such a relationship will improve our understanding of human activity effects on local and regional scale surface hydrological changes. This study has three major objectives. First, we validate the estimated ET for two forest flux tower sites using a semi-empirical Penman ET algorithm. Second, we establish a quantitative relationship between deforestation/climate variability and local-scale terrestrial ET variations by analysing changes in important surface variables that are related to terrestrial ET. Finally, we explore the effects of deforestation/climate variability on regional-scale terrestrial ET and determine the primary factors that control long-term ET variations in subarctic China.

2. Materials and Methods

2.1. Study Area

The study area is subarctic China, which is located in north-eastern China between 40.23° N and 53.57° N and between 115.53° E and 135.10° E (Figure 1). The study area has a typical continental monsoon climate with cold, dry winters and warm, wet summers. The annual mean rainfall in this area is approximately 500–600 mm, while the annual air temperature varies from −4 °C–4 °C. The topography of the study is dominated by three mountains, *i.e.*, Greater Khingan, Lesser Khingan and Baekdu Mountain; the average elevation is 1000 m above sea level, while the elevation of most other areas is approximately 500 m above sea level. Forests, croplands and grasslands constitute the main land-cover types in the study area. Since the 1980s, most deforested areas have been converted to shrublands due to the growth of the rural population; moreover, deforestation has led to flooding, soil erosion and land degradation [29].

Figure 1. Study area. LSH: Laoshan, CBS: Changbaishan.

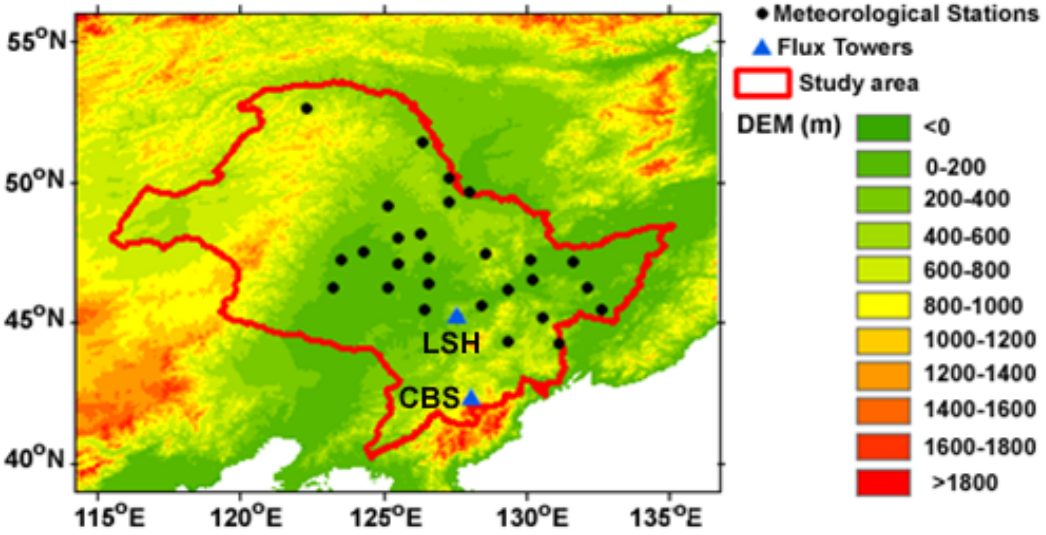

2.2. Data Sources and Data Pre-Processing

Ground-measured daily air temperature (T_a), vapour pressure (e), relative humidity (RH), wind speed (WS), precipitation (P) and atmospheric pressure (P_s) during the period 1982–2010 are obtained

from the China Administration of Meteorology (CMA), which includes 28 stations. Ground-measured ET, sensible heat flux (H), ground heat flux (G), T_a, RH, WS, e, incident solar radiation (R_s) and net radiation (R_n) derived from 2 Chinaflux tower sites (Laoshan, LSH; Changbaishan, CBS) are also obtained in this study [30–33]. The data obtained from the LSH site represent May 1 to December 31, 2002, while the data retrieved for the CBS site represent January 1 to December 31, 2003. The land-cover type at the LSH site is deciduous needleleaf forest (DNF), while the land-cover type at the CBS site is evergreen needleleaf and deciduous broadleaf mixed forest (MF). The turbulent flux data are measured according to the eddy covariance (ECOR) method. These flux datasets include half-hourly ground-measured data. When the number (N) of 30-minute measurements exceeds 40 per day, the daily average ET, R_s, RH, e, WS and T_a are the averages of the measurements [2]. Thus, the total daily ET can be calculated as follows:

$$ET = \frac{1}{N}\sum_{i=1}^{N} ET_i \times 48 \tag{1}$$

Where i is the ith 30-minute observation on each day. If N is less than 40, the daily measurements are set to a fill value. Because the ECOR method suffers from an energy imbalance problem, we use the method proposed by Twine *et al.* [34] to correct the ET values at the two sites. The corrected method is as follows:

$$ET = (R_n - G)/(ET_{EC} + H_{EC}) \times ET_{EC} \tag{2}$$

Where ET is the corrected evapotranspiration. Moreover, ET_{EC} and H_{EC} are the original evapotranspiration and the sensible heat flux measured using the EC method, respectively.

Landsat TM/ETM+ images obtained 1982 and 2000 are used to investigate the local effects of deforestation on terrestrial ET in subarctic China. These images were originally obtained during the summer (June-August), which is when forests typically have a maximum spectral disparity from other land-cover types [20]. Based on the annual forest investigation data and Statistical Yearbook data provided by the China Forestry Administration, the TM/ETM+ images are classified according to the apparent surface features into seven types, namely, forests, shrublands, croplands, grasslands, built-up areas, wetlands and water bodies. These types are delineated from the false colour composites of bands 4, 3 and 2 using on-screen digitization in the ENVI image analysis system. Among these types, the forest areas have an accuracy of approximately 90% based on field investigations. Deforestation is detected by overlaying land-cover maps in the ArcGIS software package and by analysing the forest survey data. To detect local effects of deforestation on ET, a 10 km buffer is used to produce polygons around each of the 28 meteorological stations (Figure 1). The forest changes within each buffered circle are quantified between 1982 and 2000 using statistical analysis. Moreover, the forest cover change, ΔF, around each of the 28 meteorological stations can be calculated as follows:

$$\Delta F = F_{2000} - F_{1982} \tag{3}$$

Where F_{2000} and F_{1982} refer to the forest cover amounts in 2000 and 1982, respectively. Positive values of ΔF refer to reforestation, while negative values represent deforestation. Similarly, the change in other variables (*i.e.*, ΔV, which can correspond to ΔET, $\Delta albedo$ and $\Delta NDVI$) can be calculated as:

$$\Delta V = V_{2000} - V_{1982} \tag{4}$$

Where V_{2000} and V_{1982} refer to the given variable in 2000 and 1982, respectively. When estimating regional ET, gridded meteorological datasets from the Environmental and Ecological Science Data Centre for West China are used for daily R_s, T_a, e, RH, WS, P and P_s values [35–37]. These datasets cover the period 1982–2010 on a 0.1° × 0.1° grid. Modern Era Retrospective Analysis for Research and Applications (MERRA) reanalysis meteorological data is also used to drive the SEMI-PM algorithm to verify the ET. We also use the 8-day Global Land Surface Satellite (GLASS) albedo products [38] with a resolution of 1 km and the bimonthly NDVI products provided by the Global Inventory Modelling and Mapping Studies (GIMMS) group [39] with a spatial resolution of 8 km. To better correspond with the deforestation data, the GLASS albedo and GIMMS-NDVI data are converted to a resolution of 0.1° × 0.1° using bilinear interpolation. The daily albedo and NDVI values are temporally interpolated from the 8-day and bimonthly averages using linear interpolation. Since the Multivariate El Niño/Southern Oscillation (ENSO) Index (MEI) reflects the nature of the coupled ocean-atmosphere system instead of either individual component, we also use the monthly MEI products to detect a relationship between the MEI and regional ET variability on inter-annual time scales [40].

2.3. Semi-Empirical Penman ET Algorithm

Because a semi-empirical Penman ET (SEMI-PM) algorithm proposed by [10,11] can be used for monitoring regional ET on decadal scales, this algorithm is used to estimate the effects of deforestation on ET variations in subarctic China. This algorithm considers the effects of wind speed (WS) on ET; the algorithm can be expressed as follows:

$$ET = a_1(ET_E + ET_A) + a_2(ET_E + ET_A)^2 \tag{5}$$

$$ET_E = \frac{\Delta}{\Delta + \gamma} R_s[a_3 + a_4 NDVI + RHD(a_5 + a_6 NDVI)] \tag{6}$$

$$ET_A = \frac{\gamma}{\Delta + \gamma} WS[a_7 + RHD(a_8 + a_9 NDVI)]VPD \tag{7}$$

Where $a_1 = 0.819$, $a_2 = 0.0017$, $a_3 = 0.476$, $a_4 = 0.284$, $a_5 = -0.654$, $a_6 = 0.264$, $a_7 = 3.06$, $a_8 = -3.86$, $a_9 = 3.64$, Δ is the slope of the saturated vapor pressure curve (K Pa/°C), γ is the psychrometric constant (K Pa/°C), VPD is the vapor pressure deficit (K Pa) and RHD is equivalent to 1 minus RH. In this study, we use the SEMI-PM algorithm driven by daily gridded meteorological datasets to estimate regional ET in subarctic China over the period 1982–2010.

2.4. Evaluation Method and Spatio-Temporal Analysis

The performance of the SEMI-PM ET algorithm is evaluated based on the bias and-root-mean square error (RMSE) as follows:

$$Bias = \frac{1}{M}\sum_{i=1}^{M}(E_i - M_i) \tag{8}$$

$$RMSE = \sqrt{\frac{1}{M}\sum_{i=1}^{M}(E_i - M_i)^2} \tag{9}$$

Where E_i and M_i are the estimated and measured variables, respectively, and M is the sample size. To analyse the uncertainty in the outputs of the SEMI-PM algorithm, the method of moments is used to determine the sensitivity of the SEMI-PM algorithm to variations in each of the input parameters [8]. Uncertainty in ET (S_{ET}) is represented by the propagation of the partial derivatives of the input parameters and their respective covariances:

$$s_{ET} = \sqrt{\sum[(\frac{\partial ET}{\partial x}s_x)^2 + 2r_{xy}(\frac{\partial ET}{\partial x}s_x)(\frac{\partial ET}{\partial y}s_y)]} \quad (10)$$

Where x and y represent the five input variables (*i.e.*, Rs, NDVI, RH, Ta and WS); r_{xy} is the correlation coefficient between x and y. A linear trend analysis is used to analyse the regional long-term trends in forest coverage, ET, and meteorological parameters. A simple linear regression equation is used to calculate the annual values and trends in the different variables:

$$v = at + b \quad (11)$$

Where v is the annual value of the given variable, t is the year and a is the linear trend in the given variable. The confidence levels of the derived tendencies are calculated according to Student's t-test distribution with n-2 degrees of freedom [41]:

$$t = r_{tv}\sqrt{\frac{n-2}{1-r_{tv}^2}} \quad (12)$$

Here, r_{tv} is the correlation coefficient between the original time series and the linear-fitted time series; n is the number of observations.

3. Results

3.1. ET Validation

The ground-based ET measurements from both the LSH and CBS flux tower sites are used to validate the estimated ET based on the SEMI-PM algorithm driven by daily gridded meteorological datasets for subarctic China. At the LSH site, there is good agreement between the daily estimated ET and the ground-measured ET (Figure 2). Figure 2 illustrates the root-mean-square errors (RMSEs), the biases and the square of the correlation coefficients (R^2) for the comparison between the ground-measured and estimated daily ET at both the LSH and CBS sites. The RMSEs for the LSH and CBS sites are 19.7 W/m^2 and 13.4 W/m^2, respectively. The biases for the LSH and CBS sites are 6.5 W/m^2 and 0.1 W/m^2, respectively. Moreover, the R^2 for the two sites exceed 0.9. The positive bias may be partially due to the unresolved energy balance problem in the eddy covariance datasets and the limitations of the SEMI-PM algorithm. However, at the LSH site, the model underestimates ET when the measurements are 20–70 W/m^2 and overestimates ET when the measurements exceed 100 W/m^2. It is challenging to determine the cause of the large bias at the LSH site. Instrument calibration may be a factor; we are currently attempting to compare the ET products from other algorithms.

Figure 2. Independent validation of the estimated daily evapotranspiration (ET) using SEMI-PM algorithm for (**a**) Laoshan (LSH) site and (**b**) Changbaishan (CBS) site.

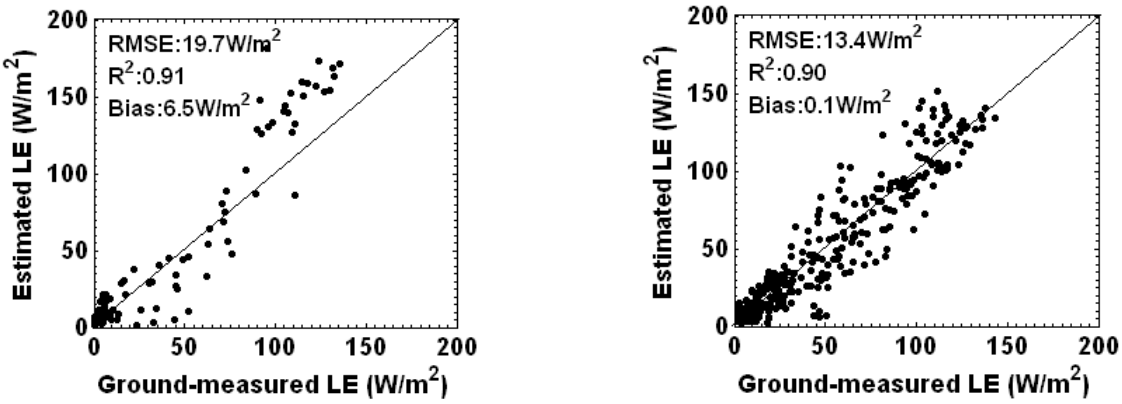

a **b**

The accuracy of the algorithm results depends largely on the accuracy of the input data. Figure 3 shows the sensitivity of the estimated ET to Rs, NDVI, RH, Ta and WS based on the method of moments. The average ET varies at the two flux towers by up to ±18% using the SEMI-PM algorithm when Rs is changed by ±20%. In response to changes in NDVI by ±20%, the estimate ET varies by ±8% at the two flux towers. Moreover, the estimate ET varies by ±20% due to changes in RH by ±6%. Similarly, ET increases by 5% for a 20% increase in T_a. The estimated ET varies by ±4% for a ±20% change in WS. Jiang *et al.* [42] reported that a reasonable upper limit for the accuracy of estimating ET using satellite data is approximately 20%. The accuracy of our validation meets this requirement.

Figure 3. Sensitivity analysis of the estimated ET with the corresponding input variables, respectively.

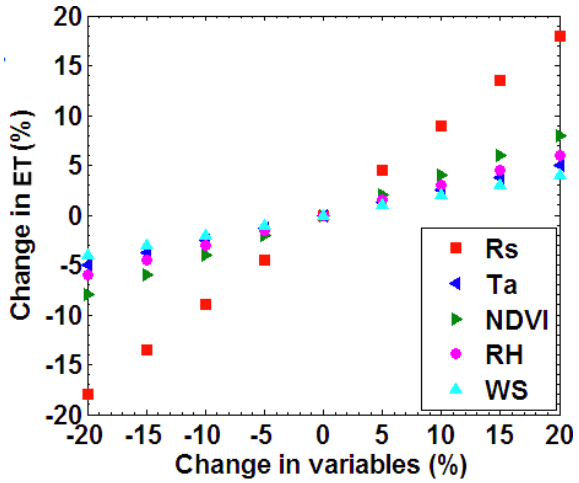

To detect long-term ET variations, a multi-annual ET validation is required [4,5,10,11]. However, the time period of the ground-based eddy covariance measurements is less than two years, which prohibits the validation of long-term ET estimates. Fortunately, Wang *et al.* [10,11] verified that the SEMI-PM algorithm is satisfactory for reproducing inter-annual variability at sites with 5 years of global FLUXNET eddy covariance data [10,11].

3.2. Local Effects of Deforestation on ET

Forest cover changes are generally correlated with annual terrestrial ET variations between 1980 and 2000. At small scales (*i.e.*, 10 km), there is positive relationship between de(re)forestation (ΔF) and annual ET variations (ΔET) at the 28 meteorological stations (Figure 4a). The relationship can be expressed as:

$$\Delta ET = 0.0377\Delta F - 2.11 \ (R^2 = 0.43, p<0.05) \quad (13)$$

In Equation (12), negative values of ΔF refer to deforestation, while positive values represent reforestation at a given station. ΔF can account for 43% of the decadal ET variations. Generally, ET decreases with increasing deforestation. ΔF directly alters the surface roughness, albedo, and the fractional vegetation cover, which determines the terrestrial *ET*. Deforestation regulates radiative forcing by increasing the surface albedo, which reduces the net shortwave radiation and the available energy. The albedo values in spring and winter are excluded due to the effects of snow cover. Figure 4b shows that there is a negative relationship between ΔF and albedo changes ($\Delta albedo$). Although this linear relationship is relatively weak (R^2 = 0.27, p = 0.1), it can explain 27% of the decadal albedo variations. Based on Figure 4b, ΔF may contribute to $\Delta albedo$. Moreover, $^{\Delta F}$-induced contributions to $^{\Delta albedo}$ may regulate changes in the absorbed energy for heating the land surface, which can partially account for the changes in ET. ΔF also affects both fractional vegetation cover and ET changes [43–46]. Generally, the fractional vegetation cover can be characterized by NDVI. Figure 4c shows a good positive relationship between ΔF and NDVI changes ($\Delta NDVI$). ΔF can explain 33% of $\Delta NDVI$ (p = 0.07) because deforestation reduces the fractional vegetation cover (or NDVI); therefore, there is a reduction in the vegetation available to transpire. Thus, deforestation leads to a local decrease in ET due to increased surface albedo and reduced vegetation cover.

Figure 4. Relationship between the deforestation and the variations in (**a**) ET, (**b**) albedo and (**c**) NDVI during 1980–2000; for x axis, positive values refers to reforestation and negative values stands for deforestation; dots stand for 28 meteorological stations.

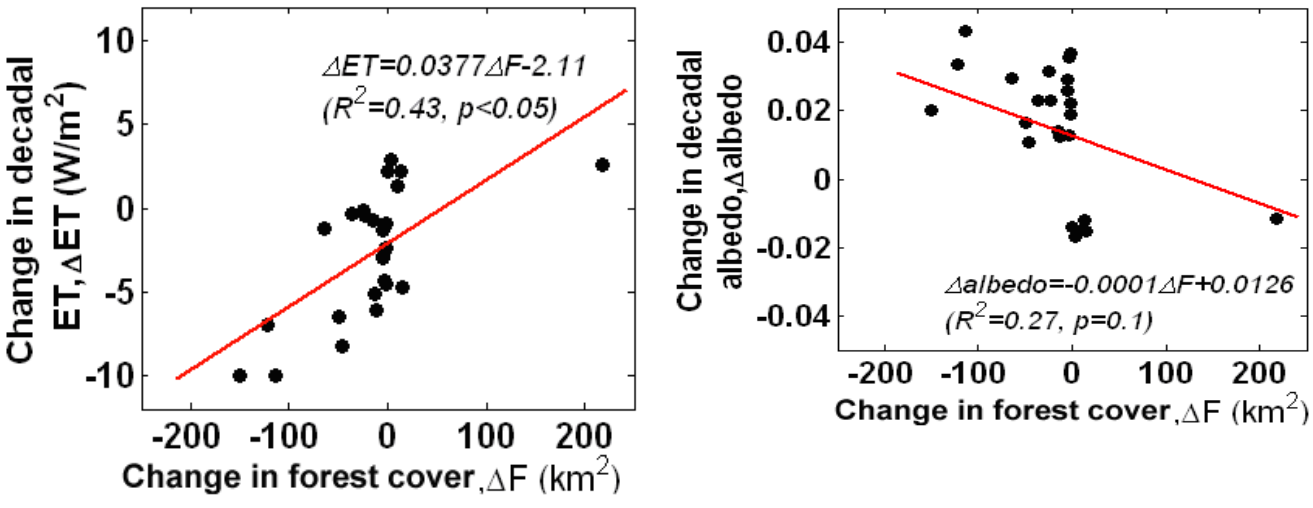

a **b**

Figure 4. *Cont.*

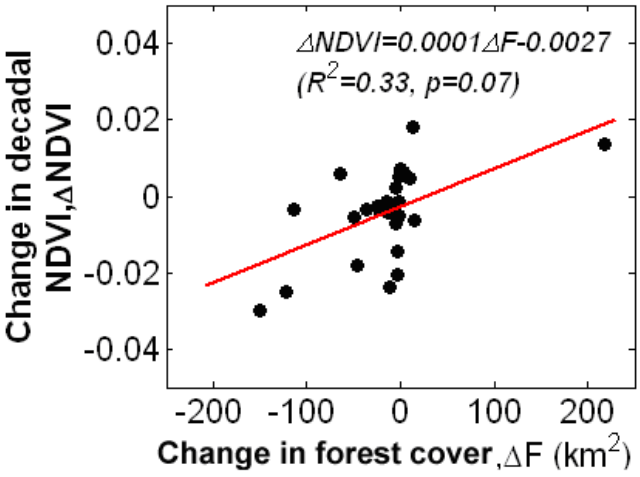

c

3.3. Regional Effects of Deforestation and Climate Change on ET

At the regional scale, dense forests decreased by approximately 9200 km^2 and sparse forests expanded by more than 830 km^2 from 1980–2000; there was a net loss of approximately 8400 km^2 [20,28]. According to the local effects of deforestation on ET, there should be a decreasing trend in ET. However, the estimated terrestrial ET results for subarctic China suggests that the terrestrial ET increased from 1982–2010 at a rate of 7.6 W/m^2 per decade ($p < 0.05$) (Figure 5). Perhaps the effects of afforestation due to human activity and climate variability offset the effects of deforestation on ET at the regional scale over this time period.

Figure 5. Relationship of forest cover and decadal ET during 1982–2000 in subarctic China (The bar graph shows the forest area. The solid and dashed lines show the annual ET and the linear trend of annual ET).

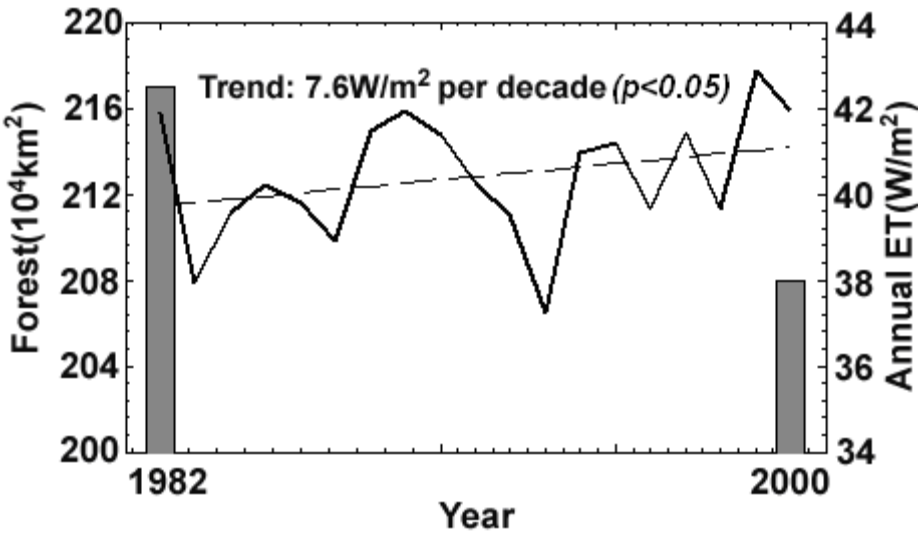

Figure 6 shows the average annual ET anomalies and the MEI for the period 1982–2010. The regional average ET for subarctic China is negatively correlated with the MEI ($r = -0.74$, $p < 0.01$). The four longest episodes (*i.e.*, 1982/1983, 1991/1992, 2002/2003 and 2008/2009) of decreasing ET correspond to four prolonged transitional periods from La Niña to El Niño conditions. However, the obvious exception is the 1997/1998 episode, which consists of a very strong El Nino that corresponds to a positive ET anomaly. This result may be partially attributed to errors in the estimated ET due to the contamination of the NDVI composite products. This contamination is caused by the high cloud cover and heavy precipitation events that occurred in 1997 in subarctic China. Figure 7 provides an example of the spatial differences in the average annual regional terrestrial ET between the La Niña and El Niño years. The annual ET is higher during La Niña events and lower during El Niño conditions. These results suggest that regional oscillations captured by the MEI can affect the annual ET via climate variability, which indicates that climate variability is the main reason for the increase in ET, while deforestation plays a secondary role in regional-scale annual ET variations in subarctic China.

Figure 6. Inter-annual variability of ET and MEI for 1982–2010.

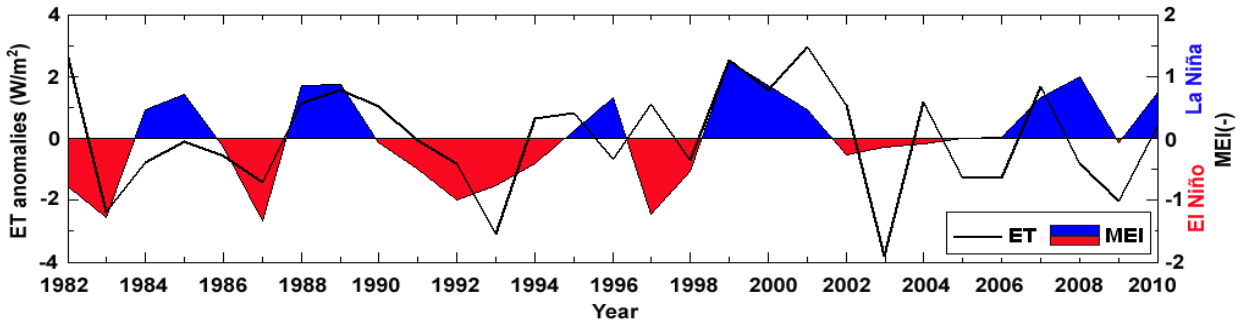

Figure 7. Spatial differences in average annual regional terrestrial ET between the El Niño and La Niña years. (**a**) the difference in annual ET between 1992 and 1991 for El Niño year, (**b**) the difference in annual ET between 2007 and 2006 for La Niña year.

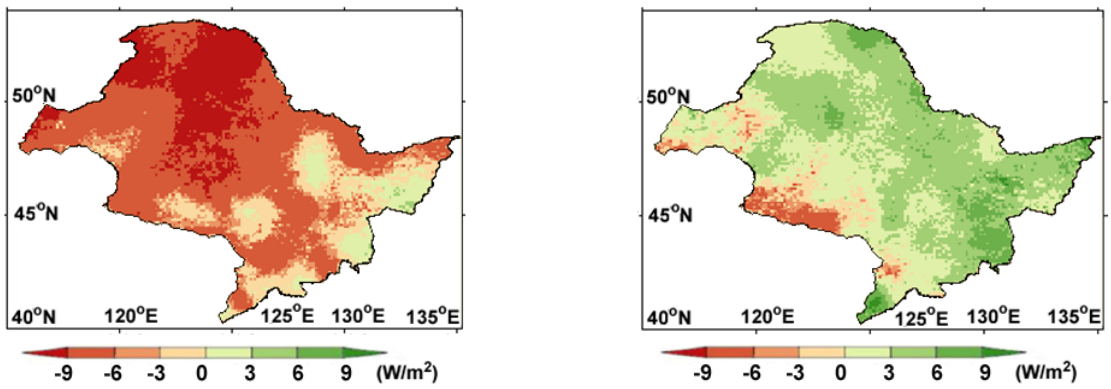

a **b**

A significant positive correlation ($r = 0.87$, $p < 0.1$) is found between the ET anomalies of and R_s. Moreover, a significant positive correlation ($r = 0.80$, $p < 0.1$) is also found between the ET anomalies and WS in subarctic China. Generally, the terrestrial ET variations are primarily controlled by the

available energy, moisture demand and atmospheric evaporative demand. R_s and WS are the two most important parameters that exhibit spatiotemporal variations in accordance with *ET* changes in boreal forest ecosystems; these parameters explain 87% of the variance in the monthly *ET* for most energy-limited regions [10,11]. In subarctic China, the spatial pattern of ET variations is strongly consistent with the spatial patterns of both R_s and WS during the period 1982–2010 (Figure 8). Other variables, such as Ta, VPD and NDVI, also affect ET variations; however, their contributions are less than those of R_s. In contrast, there is no correlation between ET variations and precipitation (P) because the study area is an energy-limited region.

Figure 8. Spatial pattern of linear trends in annual (**a**) ET, (**b**) Rs, (**c**) WS, (**d**) P, (**e**) albedo and (**f**) NDVI between 1982 and 2010.

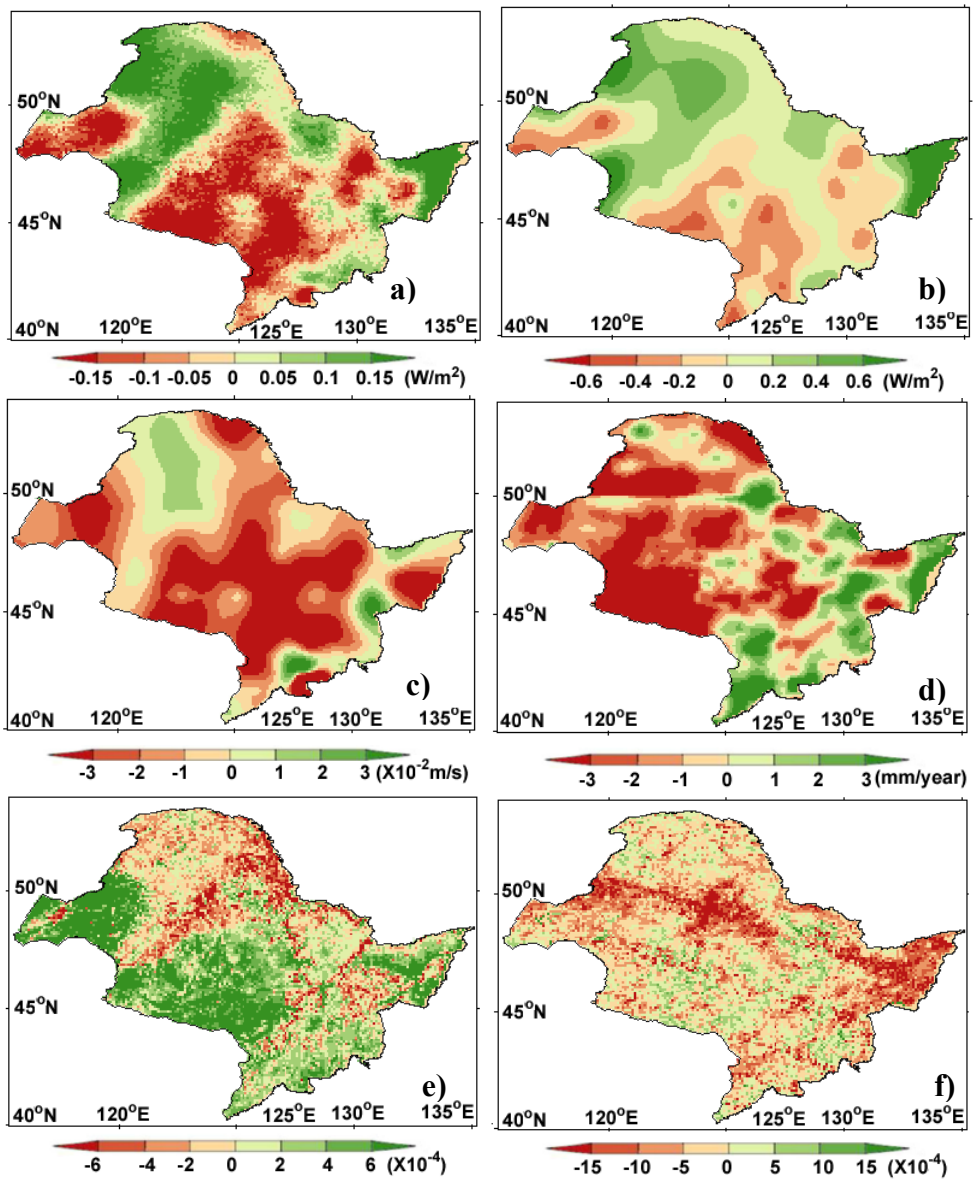

To understand the interaction between climate variability and ET changes, the effects of the MEI on the annual ET are analysed in the context of climate variability effects. Previous studies have demonstrated that during El Niño events, limitations in the terrestrial moisture supply results in

vegetation water stress and reduced evaporation; the opposite situation occurs during La Niña events [47,48].Furthermore, oscillations effect net primary production (NPP) by regulating seasonal patterns of low temperatures and moisture constraints on vegetation photosynthesis, especially for the pan-Arctic region [49]. However, in subarctic China, water stress is not a primary factor contributing to long-term ET variations. A positive correlation between the annual MEI and WS (Figure 9) is found for most regions of subarctic China, which indicates the effects of ENSO on ET via changes in WS; this result is due to evaporated moisture moving from anticyclonic to cyclonic regions [47]. It is challenging to speculate about the details of the possible interaction between ENSO and regional-scale ET changes because incident solar radiation, air temperature, precipitation, vapour pressure deficit, and land cover all contribute to ET variations. Therefore, the relationship between ENSO and ET must be examined in the future.

Figure 9. Maps of the correlation coefficients between annual MEI and WS.

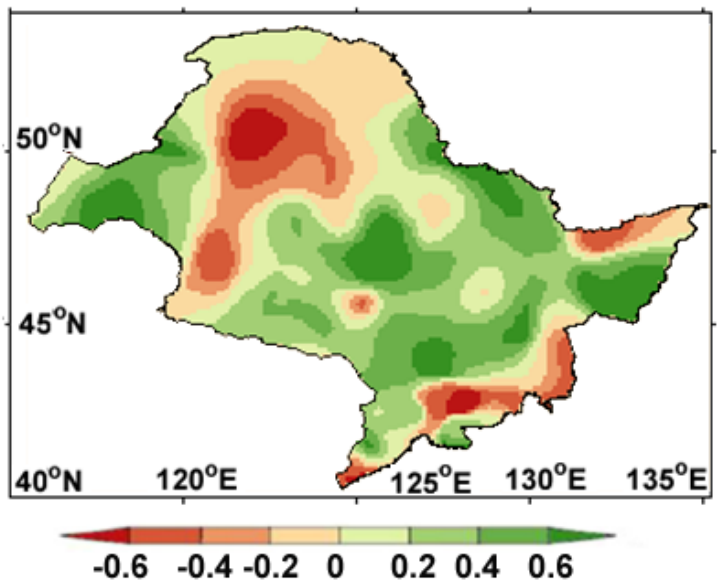

4. Discussion

4.1. Errors in the ET Estimates

Although the SEMI-PM algorithm is successfully used to estimate terrestrial ET in subarctic China, the method is still affected by input errors, the energy closure ratio of the ground-based eddy covariance measurements and the discrepancy between the gridded data and the ground-based measurements. Numerous datasets used as input for the SEMI-PM algorithm are biased compared with the ground-based measurements [2,35,50]. For example, the downward solar radiation (R_s) dataset plays an essential role in driving the SEMI-PM algorithm; however, R_s exhibits errors of approximately ±20 W/m^2 [35]. The air temperature and wind speed assimilation datasets contain small errors when driven by reanalysis forcing data [36]. In this study, a 10% error in the mean of the five inputs (*i.e.*, Rs, NDVI, RH, Ta and WS) propagates through the SEMI-PM algorithm for a mean error of 11.5%. For a 20% error in the mean of the five inputs, the SEMI-PM algorithm produces a final error of 22.1%. When MERRA data is used to drive the SEMI-PM algorithm, the resulting ET trends

are similar to those presented in Figure 4, indicating that the estimated ET results based on the SEMI-PM algorithm are robust given the uncertainty in this study.

The EC method can be considered to produce the most accurate ET estimates [51]; however, error also exists when compared with other independent ET measurements methods, such as lysimeters [2,9]. Moreover, EC-based energy measurements are frequently unconstrained; this imbalance leads to an underestimation in ET [52]. Although we corrected this problem using the method proposed by Twine *et al*. [34], uncertainties remain in the ground-based ET data. The error propagation from satellite retrievals, threshold filtering and interpolation also reduce the accuracy of ET estimates. In addition, the gap filling technique that is used for daily ground-based ET measurements also leads to large errors in the ET estimates [2]. The spatial scale mismatch between the footprint and gridded datasets (including meteorological datasets and GIMMIS-NDVI dataset) also produces discrepancies in the results. The flux tower footprint only characterizes the turbulent fluxes over approximately a few hundred meters in the vertical and horizontal directions [53]. However, the gridded datasets have coarse spatial resolution (10 km). These pixels may not capture the flux information measured at the scale of the flux tower measurements; therefore, errors are likely to be introduced in the ET estimates.

4.2. Impacts of Deforestation and Climate Change on ET

Deforestation is conducive to local-scale decreases in ET because it acts to increase surface albedo and reduce fractional vegetation cover. Previous studies have shown that deforestation decreases the amount of absorbed solar radiation at the surface [7,26]. As a result, the surface warms and ET decreases due to heat convection in boreal lands. In this study, we also verified that substantial spatiotemporal variability is present in the albedo trend, which is nearly consistent with that of the actual ET (Figure 8). Although deforestation is not the sole reason for large-scale albedo changes, it strongly affects local-scale ET.

Deforestation also reduces the fractional vegetation cover, which ultimately decreases vegetation transpiration. In this study, we also found a strong coherence between the 1982 and 2010 ET trends using the SEMI-PM algorithm and the NDVI trends in some regions. In contrast, regional-scale deforestation plays a minor role in regulating regional-scale ET variations. Moreover, there is a strong decrease in forest cover and a slight increasing trend in ET between 1982 and 2000. This change may be primarily caused by CO_2 fertilization, afforestation and global climatic changes that have eased multiple climatic constraints on plant growth and increased net primary productivity (NPP) and terrestrial ET.

Climate variability determines long-term ET variations in the northern mid-latitudes [45]. Nemani *et al*. [12] reported that recent climatic changes have increased plant growth in the northern mid-latitudes and high latitudes. Subsequently McVicar *et al*. [54] mapped the global distribution of areas where ET is energy-limited or water-limited to conclude that energy drives ET in subarctic and southern China and that changes in WS exert a larger effect in energy-limited water-yielding catchments than water-limited areas. Previous studies have shown that WS is an aerodynamic controlling variable for atmospheric evaporative demand during the ET process and contributes to long-term ET variations [55–57]. Several studies have focused on the causes of evaporative dynamics without considering WS [58–61], whereas our study illustrated the contributions of WS to ET and the

effects of ENSO on ET via changes in WS. Therefore, assessing long-term variations in regional-scale terrestrial ET requires consideration of the relationship between ENSO and WS; large uncertainties may be produced when the effects ENSO on ET are neglected.

5. Conclusions

We use meteorological data and satellite data to analyse the relationship between deforestation/climate variability and terrestrial ET variations in subarctic China. The estimated ET using a SEMI-PM algorithm and ground-based eddy covariance measurements from two forest flux tower sites illustrate that the RMSEs for the two sites are less than 20 W/m^2 and the R^2 exceed 0.9. This method can be used to detect regional-scale ET variations. At the local scale, there is positive relationship between the forest cover changes (ΔF) and annual ET variations (ΔET), namely $\Delta ET = 0.0377\Delta F - 2.11$ ($R^2 = 0.43$, $p<0.05$). This relationship is caused by deforestation-induced increases in surface albedo and a reduction in vegetation cover. However, at the regional scale, the El Niño/Southern Oscillation (ENSO) rather than deforestation dominates the multi-decadal ET variability by changing the ambient wind speed; however, the reasons for this finding require future investigations.

Acknowledgments

We gratefully acknowledge Kun Yang Institute of Tibetan Plateau Research, Chinese Academy of Sciences, Bojiang from Beijing Normal University for providing gridded meteorological and satellite data of subarctic China. The forcing dataset used in this study was developed by Data Assimilation and Modeling Center for Tibetan Multi-spheres, Institute of Tibetan Plateau Research, Chinese Academy of Sciences and this data set is provided by "Environmental & Ecological Science Data Center for West China, National Natural Science Foundation of China". Multivariate Enso Index (MEI) (interval: 1950–2011) was downloaded from this website [62]. Eddy covariance measured data for two flux tower sites in this study was downloaded from Chinaflux network [63]. This work was partially supported by the National High Technology Research and Development Program of China (2013AA122801), the National Science and Technology Support Plan During the 12th Five-year Plan Period of China (No.2012BAC19B03 and 2013BAC10B01) and the Natural Science Fund of China (41201331, 41331173 & 41301353).

Author Contributions

Yunjun Yao and Shunlin Liang prepared the manuscript. Jie Cheng, Kun Jia and Meng Liu made the remote sensing images processing. Yunjun Yao and Yi Lin contributed to the discussion.

Conflicts of Interest

The authors declare no conflict of interest.

References

1. Liang, S.; Wang, K.; Zhang, X.; Wild, M. Review of estimation of land surface radiation and energy budgets from ground measurements, remote sensing and model simulation. *IEEE J. Sel. Top. Appl. Earth Observ. Remote Sens.* **2010**, *3*, 225–240.
2. Mu, Q.; Zhao, M.; Running, S. Improvements to a MODIS global terrestrial evapotranspiration algorithm. *Remote Sens. Environ.* **2011**, *115*, 1781–1800.
3. Trenberth, K.; Fasullo, J.; Kiehl, J. Earth's global energy budget. *Bull. Am. Meteor. Soc.* **2009**, *90*, 311–323.
4. Yao, Y.; Liang, S.; Cheng, J.; Liu, S.; Fisher, J.; Zhang, X.; Jia, K.; Zhao, X.; Qin, Q.; Zhao, B.; *et al.* MODIS-driven estimation of terrestrial latent heat flux in China based on a modified Priestly-Taylor algorithm. *Agric. For. Meteorol.* **2013**, *171–172*, 187–202.
5. Yao, Y.; Liang, S.; Li, X.; Hong, Y.; Fisher, J.; Zhang, N.; Chen, J.; Cheng, J.; Zhao, S.; Zhang, X.; *et al.* Bayesian multimodel estimation of global terrestrial latent heat flux from eddy covariance, meteorological, and satellite observations. *J. Geophys. Res.* **2014**, *119*, 4521–4545, doi:10.1002/2013JD020864.
6. Yao, Y.; Liang, S.; Zhao, S.; Zhang, Y.; Qin, Q.; Cheng, J.; Jia, K.; Xie, X.; Zhang, N.; Liu, M. Validation and application of the modified satellite-based Priestley-Taylor algorithm for mapping terrestrial evapotranspiration. *Remote Sens.* **2014**, *6*, 880–904.
7. Zeng, Z.; Wang, T.; Zhou, F.; Ciais, P.; Mao, J.; Shi, X.; Piao, S. A worldwide analysis of spatiotemporal changes in water balance-based evapotranspiration from 1982 to 2009. *J. Geophys. Res.* **2014**, *119*, 1186–1202, doi:10.1002/2013 JD020 941.
8. Fisher, J.; Tu, K.; Baldocchi, D. Global estimates of the land-atmosphere water flux based on monthly AVHRR and ISLSCP-II data, validated at 16 FLUXNET sites. *Remote Sens. Environ.* **2008**, *112*, 901–919.
9. Wang, K.; Dickinson, R. A review of global terrestrial evapotranspiration: Observation, modeling, climatology, and climatic variability. *Rev. Geophys.* **2012**, *50*, doi:10.1029/2011RG000373.
10. Wang, K.; Dickinson, R.; Wild, M.; Liang, S. Evidence for decadal variation in global terrestrial evapotranspiration between 1982 and 2002. Part 1: Model development. *J. Geophys. Res.* **2010**, *115*, doi:10.1029/2009JD013671.
11. Wang, K.; Dickinson, R.; Wild, M.; Liang, S. Evidence for decadal variation in global terrestrial evapotranspiration between 1982 and 2002. Part 2: Results. *J. Geophys. Res.* **2010**, *115*, doi:10.1029/2010JD013847.
12. Nemani, R.R.; Keeling, C.D.; Hashimoto, H.; Jolly, W.M.; Piper, S.C.; Tucker, C.J.; Myneni, R.B.; Running, S.W. Climate-driven increases in global terrestrial net primary production from 1982 to 1999. *Science*. **2003**, *300*, 1560–1563.
13. Wang, K.; Dickinson, R.E.; Liang, S. Global atmospheric evaporative demand over land from 1973 to 2008. *J. Clim.* **2012**, *25*, 8353–8361.
14. Yao, Y.; Liang, S.; Xie, X.; Cheng, J.; Jia, K.; Li, Y.; Liu, R. Estimation of the terrestrial water budget over northern China by merging multiple datasets. *J. Hydrol.* **2014**, *519*, 50–68.

15. Lee, X.; Goulden, M.; Hollinger, D.; Barr, A.; Andrew Black, T.; Bohrer, G.; Bracho, R.; Drake, B.; Goldstein, A.; Gu, L.; *et al.* Observed increase in local cooling effect of deforestation at higher latitudes. *Nature* **2011**, *479*, 384–387.
16. Zhang, Y.; Liang, S. Surface radiative forcing of forest disturbances over northeastern China. *Environ. Res. Lett.* **2014**, *9*, doi:10.1088/1748-9326/9/2/024002.
17. Werth, D.; Avissar, R. The local and global effects of Amazon deforestation. *J. Geophys. Res.* **2002**, *107*, doi:10.1029/2001JD000717.
18. Findell, K.L.; Knutson, T.R. Weak simulated extratropical responses to complete tropical deforestation. *J. Clim.* **2006**, *19*, 2835–2850.
19. Medvigy, D.; Walko, R.L.; Otte, M.J.; Avissar, R. Simulated changes in northwest US climate in response to Amazon deforestation. *J. Clim.* **2013**, *26*, 9115–9136.
20. Gao, J.; Liu, Y. De(re)forestation and climate warming in subarctic China. *Appl. Geogr.* **2012**, *32*, 281–290.
21. IPCC. The physical scientific basis. *Contribution of Working Group I to the Fourth Assessment Report of the Intergovernmental Panel on Climate Change*; Cambridge University Press: Cambridge, UK, 2007.
22. Kanae, S.; Oki, T.; Musiake, K. Impact of deforestation on regional precipitation over the Indochina peninsula. *J. Hydrometeorol.* **2001**, *2*, 51–70.
23. Gedney, N.; Valdes, P. Effect of Amazonian deforestation on the northern hemisphere circulation and climate. *Geophys. Res. Lett.* **2000**, *27*, 3053–3056.
24. Bala, G.; Caldeira, K.; Wickett, M.; Phillips, T.; Lobell, D.; Delire, C.; Mirin, A. Combined climate and carbon-cycle effects of large-scale deforestation. *Proc. Natl. Acad. Sci. USA* **2007**, *104*, 6550–6555.
25. Sampaio, G.; Nobre, C.; Costa, M.; Satyamurty, P.; Soares-Filho, S.; Cardoso, M. Regional climate change over eastern Amazonia caused by pasture and soybean cropland expansion. *Geophys. Res. Lett.* **2007**, *34*, doi:10.1029/2007 GL030612.
26. Peng, S.; Piao, S.; Zeng, Z.; Ciais, P.; Zhou, L.; Li, L.; Myneni, R.; Yin, Y.; Zeng, H. Afforestation in China cools local land surface temperature. *Proc. Natl. Acad. Sci. USA* **2014**, *111*, 2915–2919.
27. Jackson, R.; Randerson, J.; Canadell, J.; Anderson, R.; Avissar, R.; Baldocchi, D.; Bonan, G.; Caldeira, K.; Diffenbaugh, N.; Field C.; *et al.* Protecting climate with forests. *Environ. Res. Lett.* **2008**, *3*, doi:10.1088/1748-9326/3/4/044006.
28. Gao, J.; Liu, Y. Climate warming and land use change in Heilongjiang Province, Northeast China. *Appl. Geogr.* **2011**, *31*, 476–482.
29. Zhang, S. Northeast timber-the pillar of new China. *Chin. Natl. Geogr.* **2008**, *576*, 240–247.
30. Yu, G.; Wen, X.; Sun, X.; Tanner, B.; Lee, X.; Chen J. Overview of ChinaFLUX and evaluation of its eddy covariance measurement. *Agric. For. Meteorol.* **2006**, *137*, 125–137.
31. Yu, G.; Fu, Y.; Sun, X.; Wen, X.; Zhang, L. Recent progress and future direction of ChinaFLUX. *Sci. China Ser. D.* **2006**, *49* (Supp. II), 1–23.
32. Yu, G.; Zhang, L.; Sun, X.; Fu, Y.; Wen, X.; Wang, Q.; Li, S.; Ren, C.; Song, X.; Liu, Y.; *et al*. Environmental controls over carbon exchange of three forest ecosystems in eastern China. *Glob. Chang. Biol.* **2008**, *14*, 2555–2571.

33. Yu, G.; Zhu, X.; Fu, Y.; He, H.; Wang, Q.; Wen, X.; Li, X.; Zhang, L.; Zhang, J.; Yan, J.; *et al.* Spatial patterns and climate drivers of carbon fluxes in terrestrial ecosystems of China. *Glob. Chang. Biol.* **2013**, *19*, 798–810.
34. Twine, T.E.; Kustas, W.P.; Norman, J.M.; Cook, D.R.; Houser, P.R.; Meyers, T.P.; Prueger, J.H.; Starks, P.J.; Wesely, M.L. Correcting eddy-covariance flux underestimates over a grassland. *Agric. For. Meteorol.* **2000**, *103*, 279–300.
35. Yang, K.; He, J.; Tang, W.; Qin, J.; Cheng, C. On downward shortwave and longwave radiations over high altitude regions: Observation and modeling in the Tibetan Plateau. *Agric. For. Meteorol.* **2010**, *150*, 38–46.
36. Chen, Y.; Yang, K.; He, J.; Qin, J.; Shi, J.; Du, J.; He, Q. Improving land surface temperature modeling for dry land of China. *J. Geophys. Res.* **2011**, *116*, doi:10.1029/2011JD015921.
37. He, J.; Yang, K. China Meteorological Forcing Dataset. Cold and Arid Regions Science Data Center at Lanzhou. **2011**, doi:10.3972/westdc.002.2014.db.
38. Liang, S.; Zhao, X.; Yuan, W.; Liu, S.; Cheng, X.; Xiao, Z.; Zhang, X.; Liu, Q.; Cheng, J.; Tang, H.; *et al.* A Long-term Global LAnd Surface Satellite (GLASS) Dataset for Environmental Studies. *Int. J. Digit. Earth.* **2013**, *6*, 5–33.
39. Tucker, C.J.; Pinzon, J.E.; Brown, M.E.; Slayback, D.A.; Pak, E.W.; Mahoney, R.; Vermote, E.F.; Saleous, N. An extended AVHRR 8-km NDVI dataset compatible with MODIS and SPOT vegetation NDVI data. *Int. J. Remote Sens.* **2005**, *26*, 4485–4498.
40. Wolter, K.; Timlin, M. El Niño/Southern Oscillation behaviour since 1871 as diagnosed in an extended multivariate ENSO index (MEI.ext). *Int. J. Climatol.* **2011**, *31*, 1074–1087.
41. Pinker, R.; Zhang, B.; Dutton, E. Do satellites detect trends in surface solar radiation? *Science* **2005**, *308*, 850–854.
42. Jiang, H.; Liu, S.; Sun, P.; An, S.; Zhou, G.; Li, C.; Wang, J.; Yu, H.; Tian, X. The influence of vegetation type on the hydrological process at the landscape scale. *Can. J. Remote Sens.* **2004**, *30*, 743–763.
43. Fisher, J.; Malhi, Y.; Bonal, D.; da Rocha, H.; de Araújo, A.; Gamo, M.; Goulden, M.; Hirano, T.; Huete, A.; Kondo, T.; *et al.* The land–atmosphere water flux in the tropics. *Glob. Chang. Biol.* **2009**, *15*, 2694–2714.
44. Miralles, D.; Holmes, T.; de Jeu, R.; Gash, J.; Meesters, A.; Dolman, A. Global land-surface evaporation estimated from satellite-based observations. *Hydrol. Earth Syst. Sci.* **2011**, *15*, 453–469.
45. Zhang, K.; Kimball, J.S.; Mu, Q.; Jones, L.A.; Goetz, S.J.; Running, S.W. Satellite based analysis of northern ET trends and associated changes in the regional water balance from 1983 to 2005. *J. Hydrol.* **2009**, *379*, 92–110.
46. Zhang, K.; Kimball, J.S.; Nemani, R.R.; Running, S.W. A continuous satellite-derived global record of land surface evapotranspiration from 1983 to 2006. *Water Resour. Res.* **2010**, *46*, doi:10.1029/2009WR008800.
47. Miralles, D.; van den Berg, M.; Gash, J.; Parinussa, R.; de Jeu, R.; Beck, H.; Holmes, T.; Jiménez,C.; Verhoest, N.; Dorigo, W.; *et al.* El Niño-La Niña cycle and recent trends in continental evaporation. *Nat. Clim. Chang.* **2014**, *4*, 122–126.

48. Trenberth, K.; Dai, A.; van der Schrier, G.; Jones, P.; Barichivich, J.; Briffa, K.; Sheffield, J. Global warming and changes in drought. *Nat. Clim. Chang.* **2014**, *4*, 17–22.
49. Zhang, K.; Kimball, J.; McDonald, K.; Cassano, J.; Running, S. Impacts of large-scale oscillations on pan-Arctic terrestrial net primary production. *Geophys. Res. Lett.* **2007**, *34*, doi:10.1029/2007GL031605.
50. Kim, H.; Hwang, K.; Mu, Q.; Lee, S.; Choi, M. Validation of MODIS 16 global terrestrial evapotranspiration products in various climates and land cover types in Asia, *KSCE J. Civil Eng.* **2012**, *16*, 229–238.
51. Baldocchi, D.; Falge, E.; Gu, L.; Olson, R.; Hollinger, D.; Running, S.; Anthoni, P.; Bernhofer, C.; Davis, K.; Fuentes, J.; *et al.* FLUXNET: A new tool to study the temporal and spatial variability of ecosystem-scale carbon dioxide, water vapor and energy flux densities. *Bull. Am. Meteorol. Soc.* **2001**, *82*, 2415–2434.
52. Wilson, K.; Goldstein, A.; Falge, E.; Aubinet, M.; Baldocchi, D. Energy balance closure at FLUXNET sites. *Agric. For. Meteorol.* **2002**, *113*, 223–243.
53. Schmid, H. Experimental design for flux measurements: Matching scales of observations and fluxes. *Agric. For. Meteorol.* **1997**, *87*, 179–200.
54. McVicar, T.; Roderick, M.; Donohue, R.; Li, L.; Van Niel, T.; Thomas, A.; Grieser, J.; Jhajharia, D.; Himri, Y.; Mahowald, N.; *et al.* Global review and synthesis of trends in observed terrestrial near-surface wind speeds: Implications for evaporation. *J. Hydrol.* **2012**, *416–417*, 182–205.
55. Krishnan, P.; Black, T.; Grant, N.; Barr, A.; Hogg, E.; Jassal, R.; Morgenstern, K. Impact of changing soil moisture distribution on net ecosystem productivity of a boreal aspen forest during and following drought. *Agric. For. Meteorol.* **2006**, *139*, 208–223.
56. Skidmore, E.; Jacobs, H.; Powers, W. Potential evapotranspiration as influenced by wind. *Agron. J.* **1969**, *61*, 543–546.
57. Chen, Y.; Xia, J.; Liang, S.; Feng, J.; Fisher, J.; Li, X.; Li, X.L.; Liu, S.; Ma, Z.; Miyata, A.; *et al.* Comparison of satellite-based evapotranspirationmodels over terrestrial ecosystems in China. *Remote Sens. Environ.* **2013**, *140*, 279–293.
58. Peterson, T.; Golubev, V.; Groisman, P. Evaporation losing its strength. *Nature* **1995**, *377*, 687–688.
59. Yao, Y.; Liang, S.; Qin, Q.; Wang, K.; Liu, S.; Zhao, S. Satellite detection of increases in global land surface evapotranspiration during 1984–2007. *Int. J. Digit. Earth.* **2012**, *5*, 299–318.
60. Lawrence, D.; Thornton, P.; Oleson, K.; Bonan, G. The partitioning of evapotranspiration into transpiration, soil evaporation, and canopy evaporation in a GCM: Impacts on land-atmosphere interaction. *J. Hydrometeorol.* **2007**, *8*, 862–880.
61. Asanuma, J.; Ishikawa, H.; Tamagawa, I.; Ma, Y.; Hayashi, T.; Qi, Y.; Wang, J. Application of the band-pass covariance technique to portable flux measurements over the Tibetan Plateau. *Water Resour. Res.* **2005**, *41*, doi:10.1029/2005WR00 3954.
62. Available online: http://www.cdc.noaa.gov/people/klaus.wolter/MEI/table.html (accessed on 26 June 2014).

63. Available online: http://159.226.111.42/pingtai/LoginRe/opendata.jsp (accessed on 26 June 2014).